Generation and application of sub-kilohertz oscillatory flows in microchannels

Giridar Vishwanathan and Gabriel Juarez*
Department of Mechanical Science and Engineering,
University of Illinois at Urbana-Champaign, Urbana, Illinois 61801, USA
(Dated: February 1, 2022)

We present a user-friendly and versatile experimental technique that generates sub-kilohertz sinusoidal oscillatory flows within microchannels. The method involves the direct interfacing of microfluidic tubing with a loudspeaker diaphragm to generate oscillatory flow in microchannels with frequencies ranging from $10-1000$ Hz and amplitudes ranging from $10-600$ μm. The speaker-based apparatus allows independent control of frequency and amplitude that is unique to the speaker's manufacturing specifications. The performance of our technique is evaluated by Fourier spectral analysis of oscillatory motion of tracer particles, obtained by particle tracking velocimetry, as well as by comparing oscillatory flow profiles against theoretical benchmarks such as Stokes flow in a square channel and Stokes' second problem near a solid boundary. Applications that utilize both the oscillatory flow and the associated steady rectified flows are demonstrated in prototypical microfluidic configurations. These include inertial focusing and mixing at low Reynolds numbers, respectively.

I. INTRODUCTION

Oscillatory flows in microfluidic devices have been shown to be useful in a range of applications such as mixing at low Reynolds numbers [1–3], particle sorting and focusing [4–7], enhancement of heat transfer [8], flow control [9, 10], microrheology [11, 12], and chemical extraction [13, 14]. Nevertheless, the widespread use and study of oscillatory flows in microchannels remains uncommon due to challenges of implementation.

At low frequencies ($0.1 \leq f \leq 10$ Hz), oscillatory flows are usually achieved by a programmed syringe pump, electromechanical relay valves [15] or a pneumatic pressure controller [16]. The fidelity of the desired waveform is limited by inertia of the oscillatory driver. For low frequencies, the response time of syringe pumps and actuators in electromechanical valves and pneumatic pressure controllers is on the order of $\mathcal{O}(10$ ms), therefore preventing the realization of sinusoidal oscillations at higher frequencies.

At high frequencies ($10^3 \leq f \leq 10^6$ Hz), piezoelectric transducers, which typically possess resonant frequencies in this range, are used [10, 14, 17–19]. The utility of piezoelectric transducers in the 10 - 1000 Hz range are limited by the small amplitudes generated. The amplitudes may be partially increased through the use of designed features such as membrane cavities in the channel on to which the piezo elements need to be bonded to be used properly [20]. More recent designs of microfluidic oscillators primarily aim to achieve oscillatory flows free of external actuators with a focus on miniaturization and integration with other lab-on-chip modules. This is typically done by exploiting non-linear fluid-elastic interaction with a membrane or diaphragm unit as a steady flow is driven through it. Therefore, a time dependent response is obtained even with a steady input at low Reynolds numbers [9, 21–23]. Other possibilities such as the use of non-Newtonian fluids for switching [24], generation of oil droplets as an oscillatory source [25], and the Coanda effect [26] have also been explored. Although these micro-oscillators are highly miniaturized, modular and in some cases, capable of producing frequencies in the audible range [21], they mostly require the fabrication of complex MEMS devices potentially discouraging their use in research attempting to use oscillatory flows. Further, in microfluidic oscillators that function based on fluid elastic interaction the amplitudes and frequencies are coupled and hence cannot be independently controlled.

Here, we describe the operation and performance of a simple plug and play apparatus capable of producing oscillatory flow in microchannels. This setup allows the user to independently control the oscillation frequency in the range of $10-1000$ Hz and amplitude in the range of $10-600$ μm. The aim of this method is simplicity and accessibility, hence, allowing researchers to implement oscillatory flow at the microscale in a convenient and cost-effective manner without the need for prior design constraints and sophisticated microfabrication.

II. EXPERIMENTAL SETUP

The apparatus is set up as displayed in the schematic, shown in Figure 1(a). A PDMS microchannel is bonded to a glass slide and observed through an inverted microscope. A loudspeaker (DROK TDA7297B, 15 W, 90 dB) is mounted next to the microscope stage. The oscillation frequency and amplitude (volume) of the loudspeaker diaphragm are controlled by a computer via an auxiliary cable. One end of microfluidic tubing (PE60 Intramedic 427416, 0.76 mm ID $\times$ 1.22 mm OD) is directly attached to the diaphragm of loudspeaker while the other end is inserted into the microchannel outlet. The tubing is main-

* Email address.; gjuarez@illinois.edu

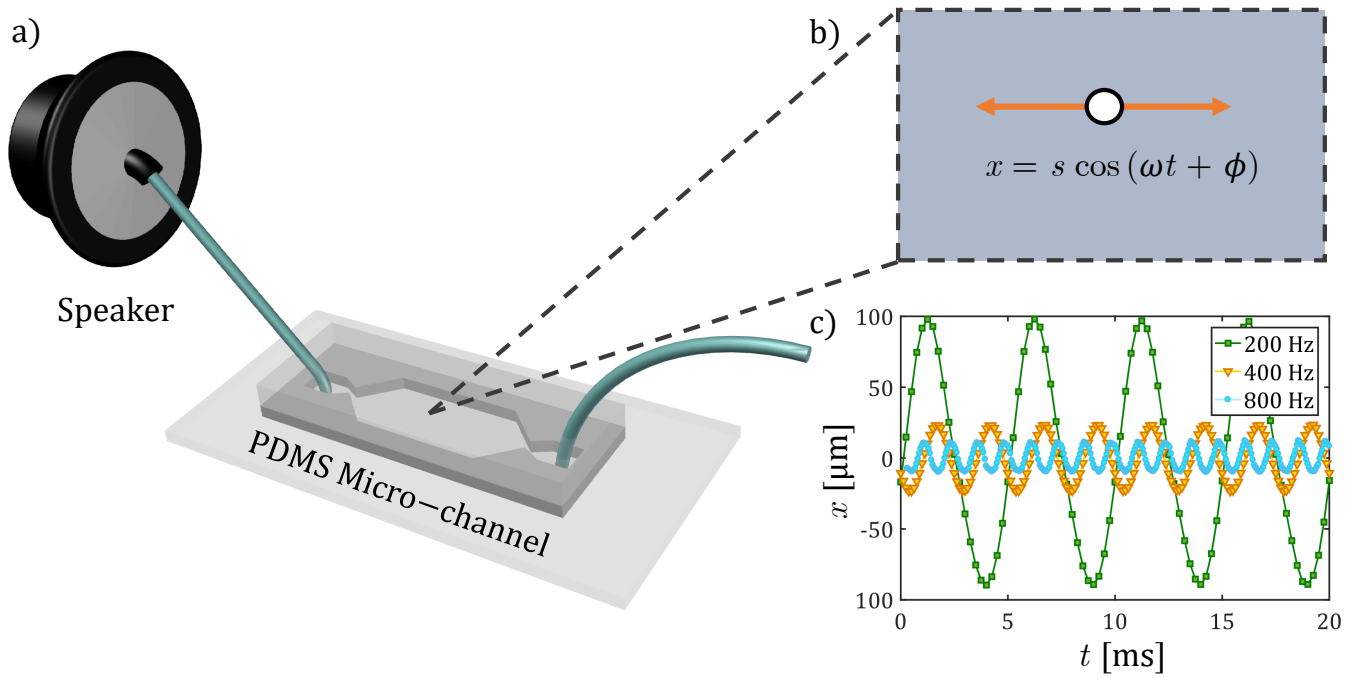

FIG. 1. (a) Schematic of the experimental setup. The loudspeaker diaphragm is directly interfaced with microfluidic tubing (maintained taut and filled with liquid) to generate sinusoidal liquid oscillations in a PDMS microchannel. (b) Schematic of tracer particle (and liquid) displacement in a microchannel described by the oscillation amplitude and angular frequency. (c) Experimental streamwise displacement of 0.93 μm diameter tracer particles in water over a number of oscillation cycles obtained with micro-particle tracking velocimetry.

tained taut and its boundary conditions correspond to a fixed end at the microchannel outlet and a forced oscillatory displacement at the diaphragm. The microchannel and the tubing are filled with liquid during operation. The oscillatory displacement of the diaphragm is transduced into elastic deformations of the microfluidic tubing at the fixed end of the device outlet. The stress induced by tubing deformation generates a time-varying pressure within, resulting in oscillatory displacement of the liquid at the same frequency (f) as the diaphragm. The streamwise displacement of a tracer particle in the channel is described by $x = s\cos(\omega t + \phi)$ and illustrated in Figure 1(b). Here, s oscillation amplitude, ω is the angular frequency, and ϕ is the initial phase.

To characterize the oscillatory flow in microchannels, tracer particles at the midplane of the microchannel were observed using brightfield illumination with objectives of 10× and 20× magnification (depth of field 8.5 μm and 5.5 μm respectively). To ensure that the tracers accurately represented the flow, polystyrene tracer particles with a mean diameter of 0.93 μm and density of 1.08 g/cm^3 were suspended in deionized water (unless mentioned otherwise). The response time associated with the tracer particles ($\tau = \rho d^2/18\mu \approx 50 \times 10^{-9}$ s) is much smaller than the oscillatory timescales considered in this study ($\tau \ll 1/f$). The particle positions were recorded using a high-speed scientific CMOS camera with frame rates exactly twenty times larger than the driving oscillation frequency ($20f$). The displacement and velocity fields are then obtained from 2D particle tracking velocimetry algorithms.

The microchannel geometries used were the following: (i) a square channel with a width and height of 110 μm and length of 5 cm, (ii) a rectangular channel with a width of 5 mm, height of 200 μm, and length of 2 cm, and (iii) a cross slot channel with square cross section with a width and height of 110 μm.

The dimensionless groups considered here are the Womersley number, the Reynolds number, and the non-dimensional oscillation amplitude. The Womersley number is the ratio of the characteristic channel width to the Stokes boundary layer thickness and is defined as $\alpha = W\sqrt{\rho\omega/\mu}$ [27]. Here, W is the channel width, ρ and μ are the liquid density and dynamic viscosity, respectively. The Reynolds number is the ratio of inertial to viscous forces of the fluid within the microchannel and defined as $\mathrm{Re} = \rho s\omega W/\mu$ [28]. Above, $s\omega$ is taken to be the characteristic liquid velocity. The non-dimensional oscillation amplitude may be expressed in terms of the Womersley and Reynolds number as $\epsilon = s/W = \mathrm{Re}/\alpha^2$. For operational conditions considered in this study, a microchannel with characteristic width of 200 μm, and DI water as the working liquid, the values of α, Re, and ϵ range from $1.5 < \alpha < 15$, $0.4 < \mathrm{Re} < 80$, and $0.1 < \epsilon < 5$, respectively.

III. RESULTS

A. Oscillatory displacement in microchannels

Examples of streamwise displacement of individually tracked particles from their mean position over a number of cycles during a 20 ms period are shown in Figure 1(c). The ratio of sampling frequency (camera framerate) to liquid oscillation frequency is kept constant at 20. That is, for oscillation at 200, 400 and 800 Hz, a framerate of 4000, 8000 and 16000 Hz is used, respectively. The corresponding amplitudes are 100, 27 and 14 μm.

The independent operational range between amplitude and frequency is shown in Figure 2(a). For a given frequency, the displacement of a tracer particle is dependent on the volume setting of the loudspeaker. As an example, three volume settings are considered here: low (30%), intermediate (60%), and high (90%), where the percentages correspond to the maximum speaker volume as determined by the computer. At 100 Hz, for example, the amplitude ranges from 50 μm at low to 800 μm at high volume setting. The amplitude swept by a tracer particle over a single oscillation period, for a given volume setting, shows a non-monotonic variation with frequency. Owing to the performance characteristics of the speaker, the maximum oscillation amplitude occurs at 200 Hz, which corresponds to the resonant frequency ($\approx$ 230 Hz) of the loudspeaker diaphragm. The horizontal black line indicates the maximum particle oscillation amplitude of 800 μm that can be measured due to the field of view limited by the camera when using a 10$\times$ microscope objective lens.

A Fourier spectrum analysis of particle trajectories at varying oscillation amplitudes and frequencies is shown in Figure 2(b). The spectra have been obtained for oscillation frequencies of 50, 200 and 800 Hz and at volume settings of low, intermediate, and high. For low and intermediate volume settings, monodisperse peaks in the spectral intensity correspond to the input driving frequency of the loudspeaker. The peaks are especially narrow at 200 Hz, or near the resonance frequency of the diaphragm. For high volume settings, the peaks correspond to the input driving frequency, however, widening of the peak is noticeable. In some cases, such as for 800 Hz at high volume setting, contributions due to higher harmonics are of considerable strength.

A quantitative measure of harmonic distortion present in the signal as compared to the fundamental driving frequency is obtained by calculating the total harmonic distortion (THD). The THD is defined as THD $= \sqrt{\Sigma_{i=1}^{N} V_i^2}/V_1$, where V_i is the power of the spectral intensity at the ith harmonic [29]. A low THD value is associated with a more accurate representation of the original driving signal. For low volume settings, the THD at 50, 200, and 800 Hz are 3.5%, 7.1%, and 9.1%, respectively. For intermediate volume settings, the THD at 50, 200, and 800 Hz are 5.2%, 8.9%, and 13.4%, respectively.For high volume settings, the THD at 50, 200, and 800 Hz are 7.3%, 11.1%, and 21.3%, respectively. The growing magnitude of higher harmonics with increasing speaker volume typically limits operation at frequencies $>$ 400 Hz to low or intermediate speaker volumes. At low frequencies however, the maximum amplitude is chosen to avoid damage to the microchannel or unfastening of the outlet tube from the speaker cone. Therefore, sinusoidal oscillations with amplitudes ranging from $10 < s < 200$ μm can be reliably achieved throughout the entire range of frequency.

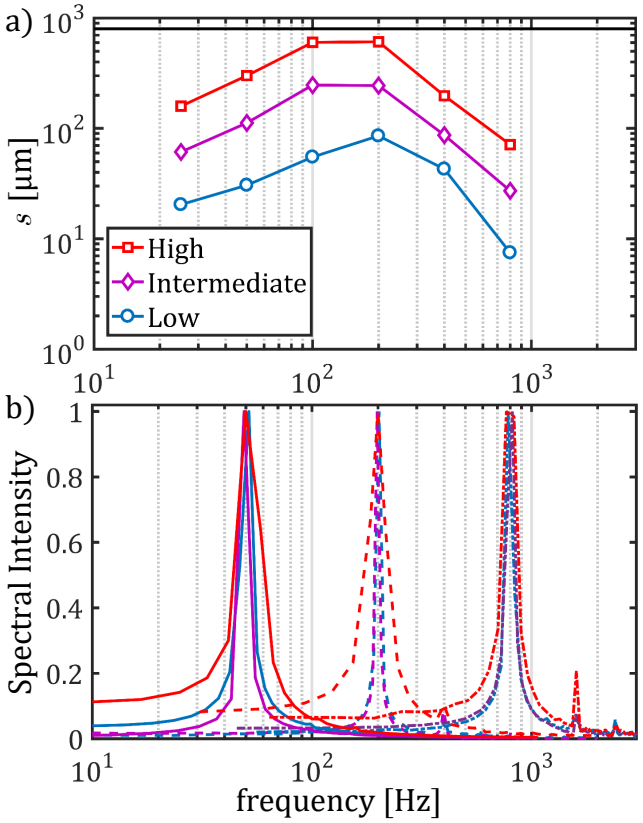

FIG. 2. (a) The amplitude of oscillatory displacement in microchannels for a range of frequencies and three amplitudes, or speaker volume settings, of low (30%, blue), intermediate (60%, magenta) and high (90%, red). (b) Fourier spectrum analysis of tracer particle displacement in the streamwise direction at three different frequencies (50, 200, and 800 Hz) and amplitudes (low, intermediate, and high).

The maximum pressure inside the square channel may be estimated from the modified Poiseuille formula:

$$\Delta P = \frac{64 \mu L s f}{D_h^2} \ , \qquad (1)$$

where D_h and L are the hydraulic diameter and length of the channel. For the square channel ($D_h = 110$ μm and $L = 5$ cm) filled with DI water ($\mu = 1.002$ mPa s) and settings for maximum oscillatory displacement ($f =$ 200 Hz, $s = 600$ μm), the pressure inside the channel is calculated to be approximately equal to 31 kPa.

B. Oscillatory flow in microchannels

The small length scales of $\mathcal{O}(100\ \mu\text{m})$ associated with microchannels imply that most microscale flows are laminar flows governed by the Stokes equation. An important feature of microscale oscillatory flows in the $10 - 1000$ Hz range is that transient effects associated with the unsteady Stokes equation become significant. An example of departure from Stokes flow is illustrated by the comparison of the steady Stokes flow velocity profile [30] at the midplane (black solid curve) against those obtained experimentally for oscillatory flow at different frequencies (symbols), shown in Figure 3(a).

To obtain the amplitude of velocity in the square channel midplane, $50 - 200$ particles ($0.93\ \mu$m diameter) are tracked for one hundred oscillation cycles and their respective velocities are computed. The amplitude of each velocity series ($U_{max}(y)$) is obtained and superposed in the streamwise direction. The resulting spread of speeds is filtered for outliers and averaged. The associated statistical error bars are smaller than the data markers shown.

The results for 100 Hz and 400 Hz are similar to the Stokes laminar flow profile (black solid curve). At 800 Hz, however, there is considerable deviation from the steady velocity profile due to increasing α with frequency. For the cases of 100, 400, and 800 Hz the α values are 2.75, 5.51, and 7.78, respectively. For these α values, the analytical series solution for the amplitude of the midplane oscillatory velocity profile ($U_{max}(y)$) was evaluated correct to one hundred terms [30], and are shown by the continuous lines to good agreement with experimental data, even at 800 Hz.

In contrast, deviations from the unsteady Stokes equation are demonstrated in Figure 3(b) by comparing the amplitude of measured oscillatory flow (symbols) in the rectangular channel ($W \gg H$), with those obtained theoretically from the solution to oscillatory flow over an infinite flat plate (Stokes' second problem) [27, 31]. The maximum temporal flow velocity as a function of distance from a flat plate is given by the expression:

$$U_{max}(y)/s\omega = \sqrt{2}e^{-y/(2\delta)}\sqrt{\cosh(y/\delta) - \cos(y/\delta)}\ , \quad (2)$$

where δ is the Stokes boundary layer length and equal to $\sqrt{\mu/\rho\omega}$.

At 800 Hz, normalized experimental data (symbols) is in good agreement with equation (2). At 50 Hz, and to a lesser extent at 200 Hz, deviations from the theory occur where the velocity amplitudes are larger than those at the far field and is detailed in the inset. This is due to the relatively short channel height ($200\ \mu$m) and the effect of boundary layers at the top and bottom walls of the channel affecting flow at the midplane. The corresponding values of α for the cases of 50, 200, and 800 Hz are 3.57, 7.14, and 14.3, respectively. Therefore, at the midplane, effects of channel side-walls may be neglected for distances larger than 4δ into the channel. Further, three dimensional flow effects can be ignored for $\alpha \geq 7.5$ when the shorter dimension is used.

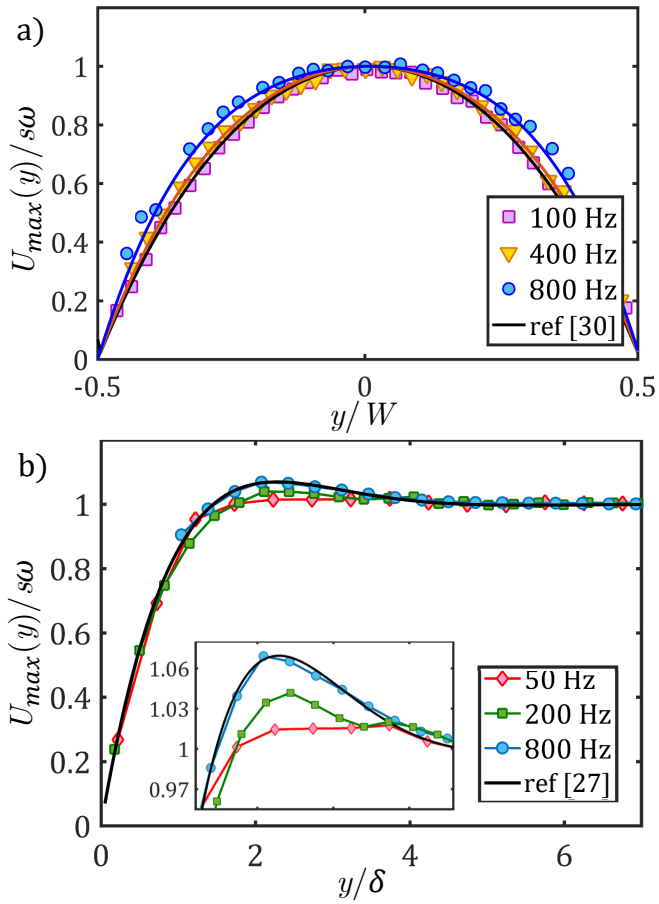

FIG. 3. (a) Oscillatory velocity flow profile in a square channel (symbols) showing deviation from Stokes flow profile (black solid curve) with increasing frequency. (b) Oscillatory velocity profile with position (symbols) near a solid channel wall in a semi-infinite rectangular channel ($W \gg H$) showing agreement with the theoretical solution (black solid curve) to Stokes' second problem [27] with increasing frequency. (Inset) Close-up of the region from $1.5 \leq y/\delta \leq 4.5$ to demonstrate agreement with equation (2) at different frequencies.

C. Applications of oscillatory flow in microchannels

The application of oscillatory flows in microchannels may be broadly divided into two categories. The first category of flows are those where oscillatory motion enables instantaneous local velocities or shear rates without net displacement, which is usually implemented to reduce device footprint and allow for prolonged observation [7, 15, 32, 33]. The second category of flows are those that utilize steady rectified flows associated with an underlying primary high frequency oscillatory flow [34], which have been shown to be useful in mixing [2], hydrodynamic manipulation of particles and cells [4, 18, 35],

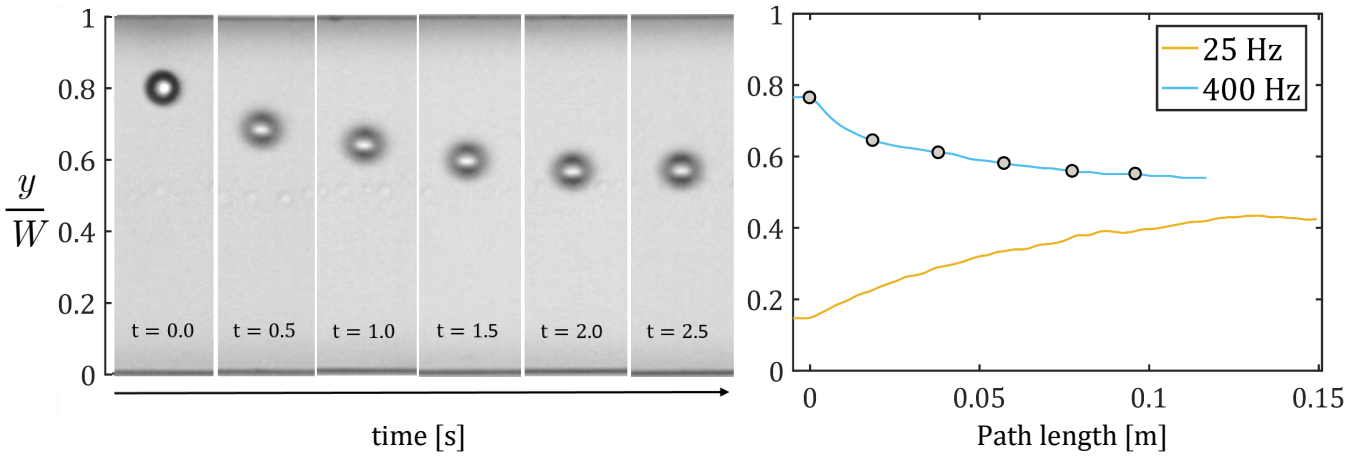

FIG. 4. (a) Inertial focusing of a 10 μm polystyrene particle in oscillatory flow with a frequency of 400 Hz in a 110 μm square channel. (b) The spanwise location of the particle centroids as they migrate to the equilibrium position at the center of the channel during oscillatory flow.

and more recently, in microrheology [11, 12]. Here, we demonstrate two specific applications of the oscillatory driver from each category, namely, inertial focusing from the former and mixing from the latter, using simple prototypical microfluidic configurations.

1. *Inertial focusing*

Inertial focusing in microchannels is a passive technique where suspended particles undergoing unidirectional flow migrate across streamlines, due to particle inertia, to equilibrium focus positions [36–39]. In straight channels, of rectangular or circular cross section, the competing forces that lead to particle migration are the wall interaction force, which directs the particle away from the channel wall, and the shear gradient force, which directs the particle toward the channel wall. The summation of these forces is termed the inertial lift and the equilibrium position of the particle is determined once the opposing forces are balanced. Factors influencing the inertial lift force are the channel geometry, flow rate, and particle size.

Since it is a high-throughput method for non-contact manipulation at the microscale, inertial focusing has been utilized in numerous applications ranging from flow cytometry [40–42], size sorting [43–45], mixing [46], and filtration [47]. An important parameter when designing channels for applications is the length required to reach the equilibrium focus position, estimated [37] to be equal to

$$L_f = \frac{\pi \mu D_h^2}{\rho U_m a^2 C_\ell} \ , \tag{3}$$

where U_m is the maximum flow velocity and C_ℓ is the lift coefficient, which typically varies in the range of $0.02 - 0.05$. From this relation, it is apparent that sufficiently high velocities and large particles are required to minimize the focusing length. Recent work, however, demonstrates the use of oscillatory flows for inertial focusing, where oscillatory flow at relatively low frequencies (< 20 Hz) results in a channel of practically infinite length [7]. Thus, it becomes possible to focus particles with far smaller particle Reynolds numbers corresponding to $\mathrm{Re_p} = (a/W)^2 \mathrm{Re} < 0.01$.

Inertial focusing of a 10 μm polystyrene particle in oscillatory flow of 400 Hz with an amplitude of 22 μm is demonstrated in the square channel, for which, $\mathrm{Re_p} = 0.050$ and $a/W = 0.091$. Micrographs of a single polystyrene particle at regular time intervals as it migrates to the equilibrium position is shown in Figure 4(a). Using stroboscopic imaging, the lateral migration toward the center of the channel is apparent. The corresponding vertical position of the particle centroid, as determined by particle tracking, is shown as a function of the approximate path length traversed by the particle in Figure 4(b). The marked points (symbols) correspond to the instances shown in the micrographs. The path length is estimated as $4sft$, where $4s$ is the distance covered by the particle at the center of the channel in a single oscillation cycle and t is the time elapsed after the start of oscillations. The focusing behavior of another particle at 25 Hz and an amplitude of 36 μm is also shown. The corresponding path length for focusing (or focus length) is found to be about 0.15 m, comparable to the 400 Hz case and in good agreement with previous results for similar conditions ($\mathrm{Re_p} = 0.050$ and $a/W = 0.125$) [7]. The time required for focusing, however, is about 3 seconds for the 400 Hz case and 35 seconds for the 25 Hz case.

The advantages of oscillatory flow for inertial focusing include decreased channel lengths, lower pressure drops, and lower shear rates. Because there is no net displacement, the particle remains in the field of view as it migrates to the equilibrium position. In contrast with uni-

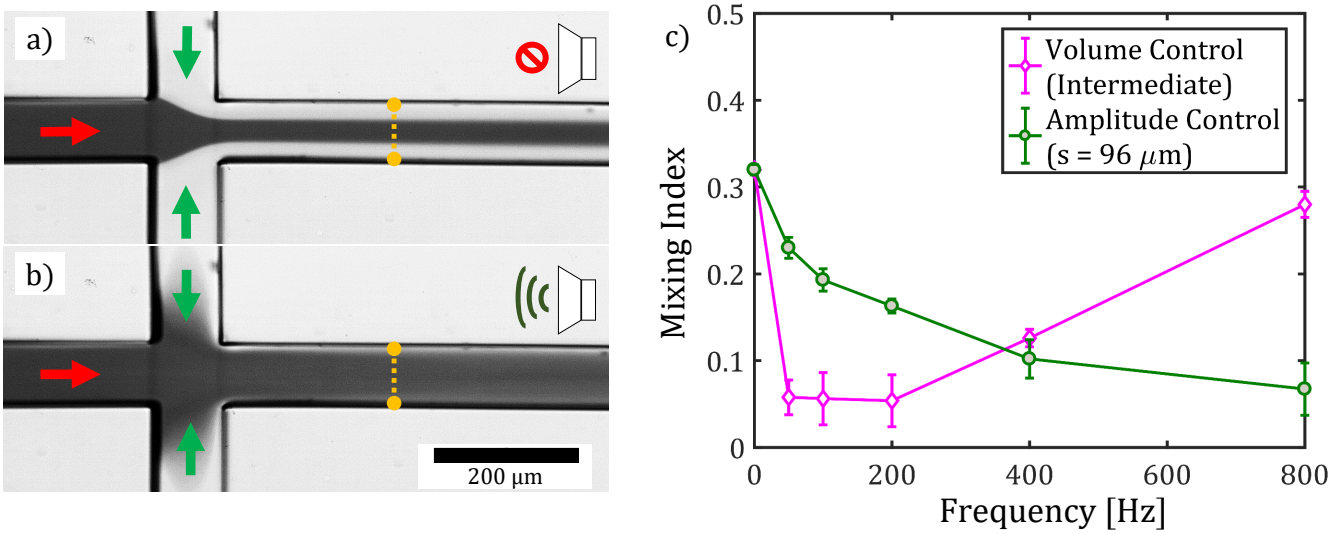

FIG. 5. (a) Mixing of co-flowing streams of 30% (w/w) aqueous glycerol solutions without oscillations applied. (b) Mixing of co-flowing streams of 30% (w/w) aqueous glycerol solutions with oscillations applied at a frequency of 400 Hz. (c) Mixing index as a function of frequency for constant amplitude and constant volume settings measured at a distance $2.5W$ downstream from the cross-slot region. Scale bar is 200 μm.

directional flow, the approximate channel length required for the particle to reach it's equilibrium position as determined by equation (3), where U_m is given by the characteristic fluid velocity $s\omega$, is $L_f \approx 1.37$ m, which is impractical. The lower pressure drop allows for the convenient fabrication and use of PDMS microchannels. The combination of lower pressure drop and lower shear rates is of particular interest in biomedical application where cells are susceptible to damage induced by fluid stresses.

2. *Microscale mixing*

Low Reynolds number (Re ≤ 1) flow in microchannels present a significant challenge to applications involving mixing [48]. This is because, the dominant mechanism of mixing is diffusion in the absence of chaotic advection, which is normally associated with high Re mixing. The effectiveness of mixing is quantified by estimating the length required to achieve mixing (L_m). For purely diffusive mixing,

$$L_m \geq D_h \mathrm{Pe} \; . \tag{4}$$

Above, Pe is the Peclet number and defined as the ratio of $U_a W/D$, where U_a is the average flow velocity and D is the diffusion coefficient. For Re ≤ 1 and diffusion coefficients of $D \approx 100$ μm^2 s^1, the Peclet number would be Pe $\geq 10^4$, resulting in a channel length for sufficient mixing to be $L_m \geq 1$ m, which is undesirable.

To overcome this challenge, a variety of microscale mixers have been developed to enhance mixing at low Re, and are categorized as either passive or active mixers [49–54]. Passive mixers make use of the channel geometry, usually incorporating repeating complex or 3D channel features to enhance mixing of two streams flowing together at a constant rate. On the other hand, active mixers rely on externally applied forces and are further categorized based on the nature of the external actuation [55]. One such category of mixers are acoustic micromixers [2, 56, 57] that rely on external acoustic actuation to generate steady rectified flows that mix different liquids.

Here, mixing of two aqueous glycerol solutions (30% w/w, $\mu = 2$ mPa s), one with colored dye and one without, is demonstrated in the cross-slot channel using steady rectified flows. As seen from figure 5(a), the dyed solution enters the cross-slot with a flow rate of 0.3 μL/min (red arrow) while the undyed solution enters the cross-slot from either side with identical flow rates of 0.15 μL/min (green arrows). This results in a total flow rate of 0.6 μL/min at the outlet.

When no oscillatory flow is imposed, minimal diffusive mixing at the interface is observed within the field of view. When oscillatory flow of 400 Hz is imposed on the same configuration, steady vortices are generated near the corners of the cross-slot as seen in Figure 5(b), which facilitate mass transfer across the interface through advection. A large exposure time of 20 ms was used for imaging so that variations over signal phase are averaged.

Mixing performance is quantified by first obtaining the intensity profile across the channel at a distance $2.5W$ downstream from the center of the cross slot, indicated by the yellow dashed lines in Figure 5(a) and (b). The standard deviation of the mixture fraction profile, derived from the intensity values, is used as the mixing index and is defined as MI $= \sqrt{\Sigma (I_i - I_m)^2/N}$, where, I_i is the pixel intensity value and I_m is the pixel intensity of a completely mixed solution, and N is the number of sampling points [58]. The values of the index range from

MI = 0.5 for completely unmixed to MI = 0 for completely mixed solutions. A value of MI $\leq$ 0.1 indicates sufficient mixing.

The variation of the mixing index as a function of frequency for both constant oscillation amplitude and constant volume setting are shown in Figure 5(c). For constant amplitude settings, the mixing index decreases monotonically with increasing frequency, implying sufficient mixing for $f \geq 400$ Hz. The improved mixing with increasing frequency is due to the increase in magnitude of the steady rectified flow velocities, which scale as $\mathcal{O}(s^2\omega)$. For a constant volume (intermediate) setting, however, the mixing index is non-monotonic, with sufficient mixing occurring in the range of $100 - 200$ Hz. Based on the amplitude characteristics, shown in Figure 2(a), for constant volume settings, the largest amplitudes occur near the resonance frequency of the loudspeaker diaphragm.

For the specific case presented here, the length demonstrated to achieve good mixing with steady rectified flows ($L_m \leq 250$ μm) is much less than the length required for mixing according to equation (4), which is calculated to be $L_m = 2.5$ cm. Although the nature of forces involved are purely hydrodynamic, oscillatory flows with independently controllable amplitude and frequency allow for the decoupling of flow rate from the rate of mixing which is not possible for passive micromixers. Additionally for the range of frequencies and amplitudes achieved here, strong rectified flows are achieved near solid boundaries in the microchannel as opposed to the boundaries of bubbles used with ultrasonic frequencies elsewhere [2, 56] which are unstable at long operation times. Lastly, the implementation of this method in combination with any other passive or active technique can further enhance mixing at the microscale by increasing the number of passes without affecting flow rate.

IV. DISCUSSION

We have discussed an accessible, effective, and versatile plug and play technique to generate oscillatory flows over a range of amplitudes and frequencies in microchannels. By directly interfacing microfluidic tubing with a loudspeaker diaphragm, sub-kilohertz oscillatory flows in the range of $10 - 1000$ Hz with amplitudes in the range of $10 - 600$ μm are produced. The corresponding wavelengths lie between $1 - 100$ m and are far larger than the dimensions of a typical microchannel. Thus, nearly unattenuated flows of a uniform phase can be achieved throughout. This is in contrast with flows in the $10^4 - 10^7$ Hz range where attenuation is significant and effects are usually local to the transducer. The resulting velocity profiles can also be tuned from Stokes-like flow ($\alpha \leq 4$) at low frequencies to plug-like unsteady Stokes flow ($\alpha \geq 7.5$) at high frequencies allowing for manipulation of the flow profile for a given micro-scale geometry. In addition to coherent oscillatory flows, strong and well defined rectified flows near curved boundaries and interfaces are also made possible in this frequency and amplitude range.

The guiding principles for applications are two-fold. First, oscillatory flows permit an increase the net distance travelled by the fluid without an accompanied increase in flow rate, shear rate, pressure drop, or particle displacement seen in long channel steady flows and high throughput applications. More generally, such conditions are particularly useful when the desired sample or analyte response to the flow environment is directionally invariant. In theory, the resulting effect can be increased indefinitely by simply increasing the frequency of oscillation. Although in practice, attenuation and secondary flows which grow stronger with increasing frequency prevent this from being realized. Owing to the large wavelengths in this range of flows, attenuation is limited while secondary flows usually become significant only for frequencies larger than 100 Hz implying that an optimum frequency is likely encountered in the range of frequencies realized here. The resulting lower steady pressure drop and steady shear rates are particularly useful for cells and other suspended biological matter that are sensitive to or potentially damaged by prolonged exposure to excessive shear rates or pressures. The absence of particle net displacement is useful in decreasing the footprint of microfluidic devices and in situations where continuous observation is needed to track the evolution in processes such as cell growth or chemical synthesis in dynamic environments.

Second, the steady rectified flow speeds are of considerable magnitude despite the maximum frequency considered being much smaller than the typical resonant frequencies of piezoelectric transducers ($1 - 100$ kHz). This is because of the large amplitudes accessed by the loudspeaker diaphragm and the dependency of flow speed on amplitude, which scales as $s^2\omega$. Further, the Stokes boundary layer thickness is accurately controlled and varies in size from $10 \leq \delta \leq 100$ μm for the highest and lowest frequencies accessed here, respectively. Therefore, the flow pathlines are less sensitive to manufacturing defects and feature surface quality, making this approach more amenable to precision applications such as sorting, trapping and manipulation of particles and cells, viscometry, and other controlled mass transfer applications.

[1] F. R. Phelan, N. R. Hughes, and J. A. Pathak, Physics of Fluids **20**, 023101 (2008).

[2] D. Ahmed, X. Mao, J. Shi, B. K. Juluri, and T. J. Huang, Lab on a Chip **9**, 2738 (2009).

[3] T. Frommelt, M. Kostur, M. Wenzel-Schäfer, P. Talkner, P. Hänggi, and A. Wixforth, Phys. Rev. Lett. **100**, 034502 (2008).

[4] R. Thameem, B. Rallabandi, and S. Hilgenfeldt, Biomicrofluidics **10**, 014124 (2016).

[5] L. Schmid, D. A. Weitz, and T. Franke, Lab on a Chip **14**, 3710 (2014).

[6] P. Marmottant and S. Hilgenfeldt, Nature **423**, 153 (2003).

[7] B. R. Mutlu, J. F. Edd, and M. Toner, Proceedings of the National Academy of Sciences **115**, 7682 (2018).

[8] J. Qu, H. Wu, P. Cheng, Q. Wang, and Q. Sun, International Journal of Heat and Mass Transfer **110**, 294 (2017).

[9] D. C. Leslie, C. J. Easley, E. Seker, J. M. Karlinsey, M. Utz, M. R. Begley, and J. P. Landers, Nature Physics **5**, 231 (2009).

[10] R. H. Phillips, R. Jain, Y. Browning, R. Shah, P. Kauffman, D. Dinh, and B. R. Lutz, Lab on a Chip **16**, 3260 (2016).

[11] G. Vishwanathan and G. Juarez, Physics of Fluids **31**, 041701 (2019).

[12] G. Vishwanathan and G. Juarez, Journal of Non-Newtonian Fluid Mechanics **271**, 104143 (2019).

[13] G. Lestari, A. Salari, M. Abolhasani, and E. Kumacheva, Lab on a Chip **16**, 2710 (2016).

[14] Y. Xie, C. Chindam, N. Nama, S. Yang, M. Lu, Y. Zhao, J. D. Mai, F. Costanzo, and T. J. Huang, Scientific Reports **5** (2015).

[15] M. Abolhasani and K. F. Jensen, Lab on a Chip **16**, 2775 (2016).

[16] Y. Zhou and C. M. Schroeder, Physical Review Fluids **1**, 053301 (2016).

[17] B. Rallabandi, C. Wang, and S. Hilgenfeldt, Physical Review Fluids **2**, 064501 (2017).

[18] V. H. Lieu, T. A. House, and D. T. Schwartz, Analytical Chemistry **84**, 1963 (2012).

[19] C. J. Morris and F. K. Forster, Micro-Electro-Mechanical Systems , 473 (2000).

[20] P. Vázquez-Vergara, A. M. T. Rojas, P. E. Guevara-Pantoja, E. C. Poiré, and G. A. Caballero-Robledo, Journal of Micromechanics and Microengineering **27**, 077001 (2017).

[21] H. M. Xia, Z. P. Wang, W. Fan, A. Wijaya, W. Wang, and Z. F. Wang, Lab on a Chip **12**, 60 (2012).

[22] S. J. Kim, R. Yokokawa, and S. Takayama, Lab on a Chip **13**, 1644 (2013).

[23] B. Mosadegh, C. H. Kuo, Y. C. Tung, Y. S. Torisawa, T. Bersano-Begey, H. Tavana, and S. Takayama, Nature Physics **6**, 433 (2010).

[24] A. Groisman, M. Enzelberger, and S. R. Quake, Science **300**, 955 (2003).

[25] P. A. Basilio, A. M. Torres Rojas, E. Corvera Poiré, and L. F. Olguín, Microfluidics and Nanofluidics **23**, 64 (2019).

[26] J. Yang, C. Chen, I. . Hu, and P. Lyu, Journal of Microelectromechanical Systems **16**, 826 (2007).

[27] L. D. Landau and E. M. Lifshits, *Fluid Mechanics, Translated by J.B. Sykes and W.H. Reid.*, Course of theoretical physics, Vol. 6 (Pergamon Press: London, 1959) pp. 83–85.

[28] C. Thomas, A. P. Bassom, P. J. Blennerhassett, and C. Davies, Proceedings of the Royal Society A: Mathematical, Physical and Engineering Sciences **467**, 2643 (2011).

[29] D. Shmilovitz, IEEE Transactions on Power Delivery **20**, 526 (2005).

[30] V. O'Brien, Journal of the Franklin Institute **300**, 225 (1975).

[31] C. Y. Wang, Applied Mechanics Reviews **42**, 269 (1989).

[32] K. Jo, Y.-L. Chen, J. J. de Pablo, and D. C. Schwartz, Lab on a Chip **9**, 2348 (2009).

[33] M. Alizadehgiashi, A. Khabibullin, Y. Li, E. Prince, M. Abolhasani, and E. Kumacheva, Lab on a Chip **9**, 2738 (2009).

[34] N. Riley, Annual Review of Fluid Mechanics **33**, 43 (2001).

[35] B. R. Lutz, J. Chen, and D. T. Schwartz, Analytical Chemistry **78**, 1606 (2006).

[36] D. Di Carlo, D. Irimia, R. G. Tompkins, and M. Toner, Proceedings of the National Academy of Sciences **104**, 18892 (2007).

[37] D. Di Carlo, Lab on a Chip **9**, 3038 (2009).

[38] J. M. Martel and M. Toner, Annual Review of Biomedical Engineering **16**, 371 (2014).

[39] D. Stoecklein and D. Di Carlo, Analytical Chemistry **91**, 296 (2019).

[40] S. C. Hur, H. T. K. Tse, and D. D. Carlo, Lab on a Chip **10**, 274 (2010).

[41] A. A. S. Bhagat, S. S. Kuntaegowdanahalli, N. Kaval, C. J. Seliskar, and I. Papautsky, Biomedical Microdevices **12**, 187 (2010).

[42] J. Oakey, R. W. Applegate, E. Arellano, D. D. Carlo, S. W. Graves, and M. Toner, Analytical Chemistry **82**, 3862 (2010).

[43] S. S. Kuntaegowdanahalli, A. A. S. Bhagat, G. Kumar, and I. Papautsky, Lab on a Chip **9**, 2973 (2009).

[44] L. Wu, G. Guan, H. W. Hou, A. A. S. Bhagat, and J. Han, Analytical Chemistry **84**, 9324 (2012).

[45] N. Nivedita and I. Papautsky, Biomicrofluidics **7**, 054101 (2013).

[46] H. Amini, E. Sollier, W. M. Weaver, and D. D. Carlo, Proceedings of the National Academy of Sciences **109**, 11593 (2012).

[47] J. Seo, M. H. Lean, and A. Kole, Applied Physics Letters **91**, 033901 (2007).

[48] J. M. Ottino and S. Wiggins, Philosophical Transactions of the Royal Society A **362**, 923 (2004).

[49] V. Hessel, H. Löwe, and F. Schönfeld, Chemical Engineering Science **60**, 2479 (2005).

[50] N. T. Nguyen and Z. Wu, Journal of Micromechanics and Microengineering **15**, R1 (2005).

[51] C. Y. Lee, C. L. Chang, Y. N. Wang, and L. M. Fu, International Journal of Molecular Sciences **12**, 3263 (2011).

[52] K. Ward and Z. H. Fan, Journal of Micromechanics and Microengineering **25**, 094001 (2015).

[53] C. Y. Lee, W. T. Wang, C. L. Chang, and L. M. Fu, Chemical Engineering Journal **288**, 146 (2016).

[54] G. Cai, L. Xue, H. Zhang, and J. Lin, Micromachines **8**, 274 (2017).

[55] T. J. Ober, D. Foresti, and J. A. Lewis, Proceedings of the National Academy of Sciences **112**, 12293 (2015).

[56] R. H. Liu, J. Yang, M. Z. Pindera, M. Athavale, and P. Grodzinski, Lab on a Chip **2**, 151 (2002).

[57] H. Bachman, H. Fu, P. hsun Huang, Z. Tian, J. Embry-Seckler, J. Rufo, Z. Xie, J. H. Hartman, S. Zhao, S. Yang, J. N. Meyer, and T. J. Huang, Lab on a Chip **19**, 2404 (2019).

[58] R. H. Liu, M. A. Stremler, K. V. Sharp, M. G. Olsen, J. G. Santiago, R. J. Adrian, H. Aref, and D. J. Beebe, Journal of Microelectromechanical Systems **9**, 190 (2000).